JOM, Vol. 68, No. 12, 2016
DOI: 10.1007/s11837-016-2059-y

Progress on Numerical Modeling of the Dispersion of Ceramic Nanoparticles During Ultrasonic Processing and Solidification of Al-Based Nanocomposites

DAOJIE ZHANG[1] and LAURENTIU NASTAC[1,2]

1.—The University of Alabama, Tuscaloosa, AL 35487, USA. 2.—e-mail: lnastac@eng.ua.edu

In present study, 6061- and A356-based nano-composites are fabricated by using the ultrasonic stirring technology (UST) in a coreless induction furnace. SiC nanoparticles are used as the reinforcement. Nanoparticles are added into the molten metal and then dispersed by ultrasonic cavitation and acoustic streaming assisted by electromagnetic stirring. The applied UST parameters in the current experiments are used to validate a recently developed magneto-hydro-dynamics (MHD) model, which is capable of modeling the cavitation and nanoparticle dispersion during UST processing. The MHD model accounts for turbulent fluid flow, heat transfer and solidification, and electromagnetic field, as well as the complex interaction between the nanoparticles and both the molten and solidified alloys by using ANSYS Maxwell and ANSYS Fluent. Molecular dynamics (MD) simulations are conducted to analyze the complex interactions between the nanoparticle and the liquid/solid interface. The current modeling results demonstrate that a strong flow can disperse the nanoparticles relatively well during molten metal and solidification processes. MD simulation results prove that ultrafine particles (10 nm) will be engulfed by the solidification front instead of being pushed, which is beneficial for nano-dispersion.

INTRODUCTION

Micron-sized ceramic particle reinforcements are widely used in aluminum-based metal matrix composites (MMCs) which have high strength-to-weight ratios and enhanced mechanical and thermal properties, including specific modulus, superior strength, stiffness, good wear resistance, fatigue resistance and improved thermal stability.[1–4] More recently, to overcome the counterpart that the ductility of the MMCs deteriorates with high ceramic particle concentration,[5] more attention has been drawn to metal matrix nanocomposites (MMNCs), since the properties of metallic alloys reinforced by ceramic nanoparticles (with dimensions less than 100 nm) would be enhanced considerably while the ductility of the matrix is retained.[6–12] However, it is extremely difficult to obtain uniform dispersion of nano-sized ceramic particles in liquid metals due to their high viscosity, poor wettability in the metal matrix, and a large surface-to-volume ratio, which results in agglomeration and clustering.[5] Currently, several fabrication technologies including high-energy ball milling,[9,12] in situ synthesis,[8] electroplating,[13] and ultrasonic technology (UST)[5,6] are most commonly used, among which UST is supposed to be more reliable and cost effective.

Induction heating, which is a clean, energy-efficient and well-controllable melting process, is widely applied in the metallurgical industry. During the process, the dominant electromagnetic field will generate heat (affecting the temperature field) and momentum (controlling the fluid flow field). Meanwhile, all these three fields may strongly influence one another, which may significantly complicate the problem.[14] An improved understanding of the heat and electromagnetically driven flow mostly requires mathematical modeling, as experimental studies, especially for high-temperature materials processing, may be restricted because of the physical and chemical properties of the melts.[15]

During the solidification process, the particles will either be pushed or engulfed by the solidification front, among which particle pushing will always lead to segregation and even clustering of the particulate reinforcement, which is undesirable as it results in non-homogeneous response and lower macroscopic mechanical properties. In general, it is considered that whether particles are pushed or engulfed during solidification depends on the velocity of the particle relative to the solidification front according to several previous models describing such particle engulfment and pushing phenomena.[16–20]

However, it is extremely expensive and difficult, perhaps impossible, to investigate the interfacial properties experimentally at the atomic level. Thus, molecular dynamics (MD) simulations (atomistic simulations) conducted at the atomic level offer a good alternative in studying the interface mechanics.

In this study, the ANSYS Fluent Dense Discrete Phase Model (DDPM)[21] was adapted. The DDPM accounts for turbulent fluid flow, heat transfer, electromagnetic forces, and complex interactions between the molten alloy and nanoparticles during the melting and unidirectional solidification processes. Based on the theory proposed by Ferguson, all of the nanoparticles are assumed to be engulfed by the solidification front and no entrapment will occur. The dispersion of SiC nanoparticles with different fluid flow intensities, and with and without induction stirring, has been investigated in detail. The open source MD program Large-scale Atomic/Molecular Massively Parallel Simulator (LAMMPS)[22] is used to conduct MD simulations to analyze the complex interactions between the nanoparticle and the liquid/solid interface.

MODEL DESCRIPTION

A MHD model has been developed in ANSYS Maxwell and ANSYS Fluent. The Lorentz force density was obtained in Maxwell and then interpolated on the Fluent finite volume mesh and used as momentum source in solving the fluid flow.

Electromagnetic Field and CFD Model

The geometries of the electromagnetic field and computational fluid dynamics (CFD) model are shown in Fig. 1. Two dimensional (2D) axisymmetric models are applied to calculate the electromagnetic forces and the CFD-related computations. The induction furnace is comprised of an Al_2O_3 crucible and 3 Cu induction coils. An electric current of 200 A with frequency of 50 Hz is passed through the coils to induce eddy currents in the liquid aluminium alloys. All material properties required for EM modeling are available in ANSYS Maxwell.

The ultrasonic probe has a diameter of 40 mm. The liquid aluminium alloy is 6061. It has a density of 2685 kg/m^3. The SiC nanoparticles with an average particle size of 55 nm and density of 3216 kg/m^3 are treated as inert-particles. The mass flow rate of the SiC nanoparticles is 0.014 kg/s. Thus, 1.0 wt.% of SiC nanoparticles can be injected at about 15 mm beneath the ultrasonic probe for 1 s. The multiphase CFD model accounts for turbulent fluid flow, heat transfer, and the complex interaction between the molten alloy and nanoparticles by using the ANSYS Fluent DDPM and k–ω turbulence model.[21]

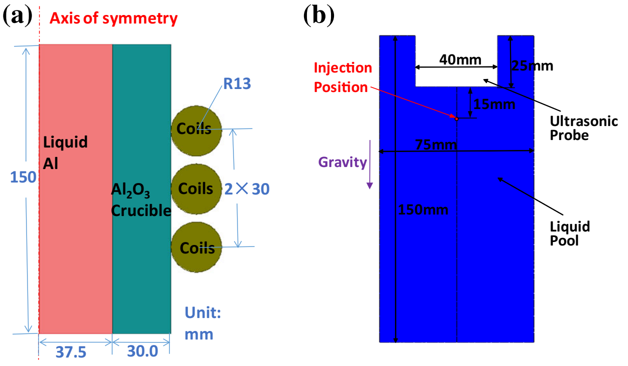

Fig. 1. Geometry model: (a) electromagnetic field; (b) CFD model.

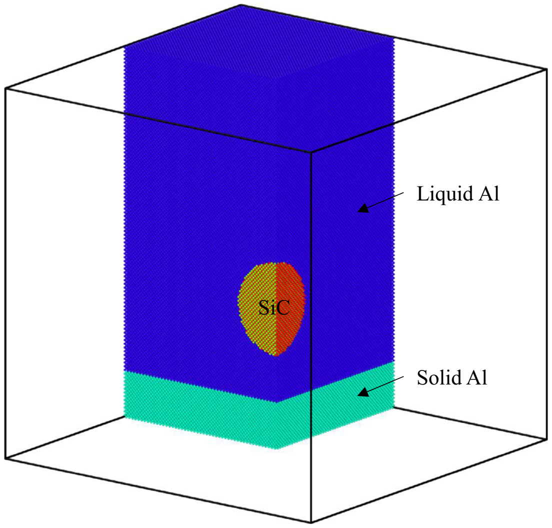

Fig. 2. MD geometry model.

The electromagnetic field model, fluid flow model, solidification model, particle tracking model, and solution procedure are presented in detail in Refs. 23–25.

Molecular Dynamics Model

A quarter of the MD geometry model is shown in Fig. 2. The dimensions in the x, y, and z directions are 40 nm × 40 nm × 40 nm. The diameter of the SiC nanoparticle is 10 nm. The simulated structure of pure aluminum is a face-centered cubic (FCC) structure with a lattice parameter of 4.05 Å and with the $<100>$ direction coincident with the Cartesian coordinates, since planes of looser packing, such as {100}, are better able to accommodate an atom that leaves the liquid to join the solid than a closer packed plane, such as {111}.[26] The nanoparticle consists of a cubic crystalline polytype of silicon carbide (3C-SiC) with a lattice parameter of 4.36 Å.[27] In total, 3,900,208 atoms are generated.

In the study, the free solidification technique is utilized to simulate the solidification process. Periodic boundary conditions are applied in three coordinate directions. The simulation starts with a solid SiC region, a solid Al region (thickness 5 nm in the z direction) and a liquid Al region separated by a nominally flat liquid–solid boundary. The two-phase Al system is established by holding the atoms fixed in the solid Al region of the original crystalline lattice and melting the liquid Al region by raising the temperature to some temperature above the melting point. Upon solidification, both the solid Al atoms at the bottom and the liquid Al atoms at the top can move freely into each other because of the periodic boundary conditions. The velocity of the atoms is then rescaled to some temperature below the melting point. Due to the density difference between solid and liquid, constant volume simulations will lead to a gradual build-up of pressure during crystallization which eventually halts solidification.[28] Instead, constant pressure conditions are required with the pressure maintained at zero throughout the run with a time step of 1 fs. During solidification, the solid atoms at the bottom which were initially fixed in position are allowed to move. The simulation is terminated when complete solidification is achieved (about 600 ps).

Interatomic potentials for aluminum, silicon carbide and the interface are discussed in the following sections.

EAM Potential for Aluminum

In this study, the embedded atom method (EAM) developed by Mishin et al.[29] as shown in Eq. 1 is used to simulate bulk aluminum. A cut-off distance rc = 6.365 Å is used.[30]

$$E_{\mathrm{tot}} = \frac{1}{2}\sum_{ij} V(r_{ij}) + \sum F(\bar{\rho}_i), \tag{1}$$

$$\bar{\rho}_i = \sum_{j\neq i} \rho(r_{ij}), \tag{2}$$

where $V(r_{ij})$ is the pair potential as a function of the atomic separation distance r_{ij} between two atoms i and j, F is the embedding energy as a function of the density $\bar{\rho}_i$, which is induced on atom i by all other atoms in the system, and $\rho(r_{ij})$ is the atomic density function. The interatomic potentials for Al are available from Ref. 30.

Tersoff Many-Body Potential for Silicon Carbide

The Tersoff potential V_{ij} in the simplest sense is composed of the attractive and repulsive interactions present in a bond as shown in Eq. 3.

$$V_{ij} = f_{\mathrm{C}}(r_{ij})\left[\left(f_{\mathrm{R}}(r_{ij}) + b_{ij} f_{\mathrm{A}}(r_{ij})\right)\right], \tag{3}$$

where the subscript R and A correspond to the repulsive and attractive component of the potential. The potential is a function of b_{ij}, two energy constants and $f_{\mathrm{R}}(r_{ij})$, $f_{\mathrm{A}}(r_{ij})$ and $f_{\mathrm{C}}(r_{ij})$, which are functions representing the potential associated with the repulsive, attractive and cut-off functions. These functions are dependent on the length of the bond. In the aforementioned equations the subscripts i and j label the atoms of the system, and r_{ij} is the length of the ij bond. The necessary equations along with the energy constants and corresponding cut-off distances for silicon carbide are summarized in Tersoff.[31,32]

Potential for Describing the Interface

Ideally, any interatomic potential model employed for representing the interface should include two-body and three-body interactions. Two-body interactions are the interaction between Al–Si and Al–C, while three-body interactions involve Al–Si–C, Al–C–Si, Al–Si–Al and Al–C–Al. In this study, in order to simplify the simulation procedure and in turn reduce the computational time, a two-body pair-wise potential is used.

Two popular potentials, Lennard–Jones (LJ) potential and Morse potential, are usually used to model the Al–SiC interface. But according to Dandekar and Shin,[26] the Morse potential values parameterized from ab initio data are able to best represent the current system and is therefore used in this study to represent the interface.

$$V = D_0\left[e^{-2\alpha_m(r-r_0)} - 2e^{-\alpha_m(r-r_0)}\right], \tag{4}$$

where r is the distance between the atoms, r_0 is the equilibrium bond distance, D_0 is the well depth of the potential, α_m is the width of the potential, and V is the interatomic potential. The parameters are summarized in Table I.[33]

SIMULATION RESULTS AND DISCUSSION

Figure 3a and b shows the fluid flow with electromagnetic stirring (EMS) and UST only, respectively. As can be seen, the flow with EMS only consists of two axisymmetric recirculating loops,

Table I. Morse potential function parameters parameterized to the ab initio data obtained

System	Parameters	Morse potential
Al–Si	D_0 (eV)	0.4824
	α (1/Å)	1.322
	r_0 (Å)	2.92
Al–C	D_0 (eV)	0.4691
	α (1/Å)	1.738
	r_0 (Å)	2.246

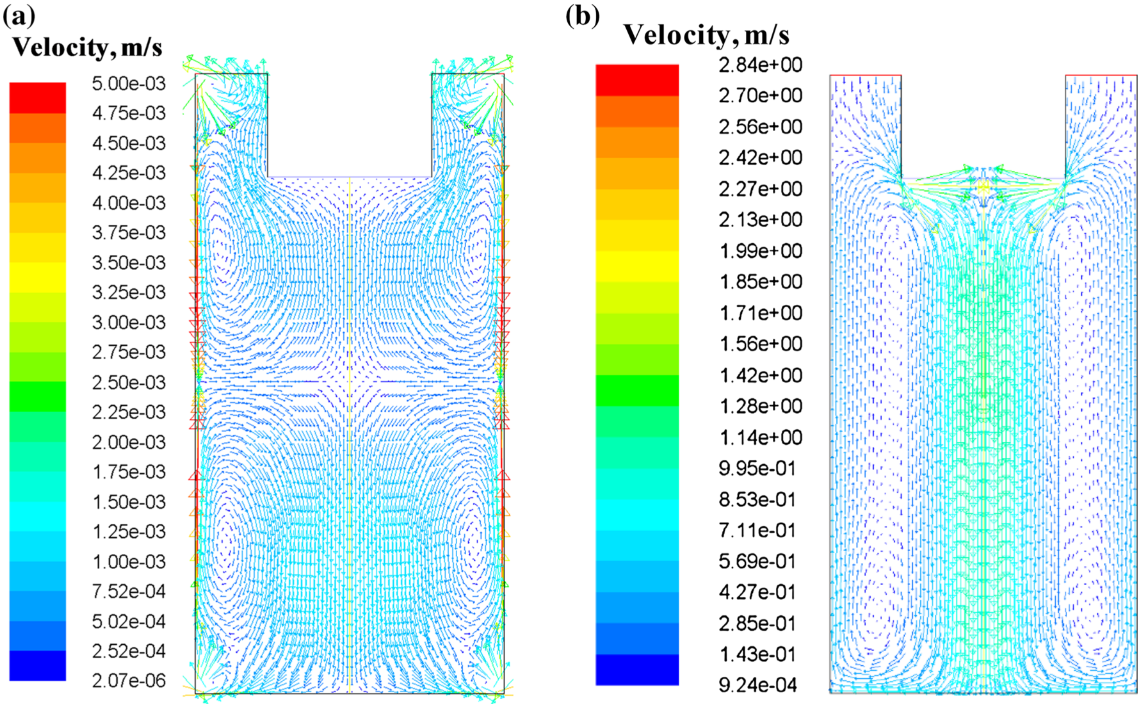

Fig. 3. Comparison between fluid flow with (a) EMS only and (b) UST only.

consistent with the computed curl of the EM force field. Also, the magnitude of maximum velocity induced by the EMS is 5×10^{-3} m/s, which is much lower than that induced by the UST which is 2.84 m/s.

When the induction stirring is taken into consideration, the fluid flow and particle distributions after 1.0 s and 3.0 s are shown in Fig. 4, respectively. Compared to the results without EMS (Figure 3 in Ref. 24), the fluid flow pattern is basically the same, because the induced flow by induction stirring is relatively weak compared to that induced by ultrasonic stirring. But there are still some differences especially at the center of the furnace where the flow at the bottom becomes weaker than that at the top because of the induction stirring. It can also be seen that there are considerable numbers of particles in the center of the furnace, which indicates that the particle distribution becomes even better than before. This can be explained by the induction stirring modifying the fluid flow, making it more uniform.

Figure 5 shows the fluid flow and particle distributions after 10.0 s and 30.0 s with EMS during the solidification process, respectively. As can be seen, when solidification starts, the fluid flow is damped in the mushy zone, and particles approaching the solidification front are captured. As can be seen in Fig. 5d that, after 20 s, the nanoparticles are dispersed quite well throughout the metal matrix, which is also validated by SEM analysis.[34,35] Generally speaking, the fluid flow and nanoparticle distributions do not change too much compared with the results without EMS (Figure 3 in Ref. 24).

In order to perform a more detailed particle distribution analysis, the geometry is divided into 150 slices (1 mm each) along the vertical direction and 75 slices (0.5 mm each) along the radial direction, thus there are 11,250 cells in total (including the probe area). The numbers of particles in each slice and cell are counted. Particle distributions along vertical and radial direction after 3 s, 10 s and 30 s, and overall particle distribution after 30 s are shown in Figs. 6, 7 and 8, respectively.

It can be seen from Fig. 6 that the distribution along the vertical direction after 3 s is very uniform. As solidification starts, more and more particles are captured by the solidification front, thus there are fewer and fewer particles on the top of the furnace (away from the solidification area). In Fig. 7, generally along the radial direction, further away from the symmetry, more particles are present. However, there is a peak in the middle area because of the flow vertex. Moreover, a more intuitive observation of the overall particle distribution can be obtained from Fig. 8.

In the study, we use the centro-symmetry parameter (CSP) to discriminate between "liquid" and "solid" atoms in the cell. In solid-state systems, the centro-symmetry parameter (CSP) developed by Kelchner et al.[36] is a useful measure of the local lattice disorder around an atom and can be used to characterize whether the atom is part of a perfect lattice, a local defect (e.g., a dislocation or stacking fault), or at a surface.[22] The CSP of an atom having N nearest neighbors is defined as

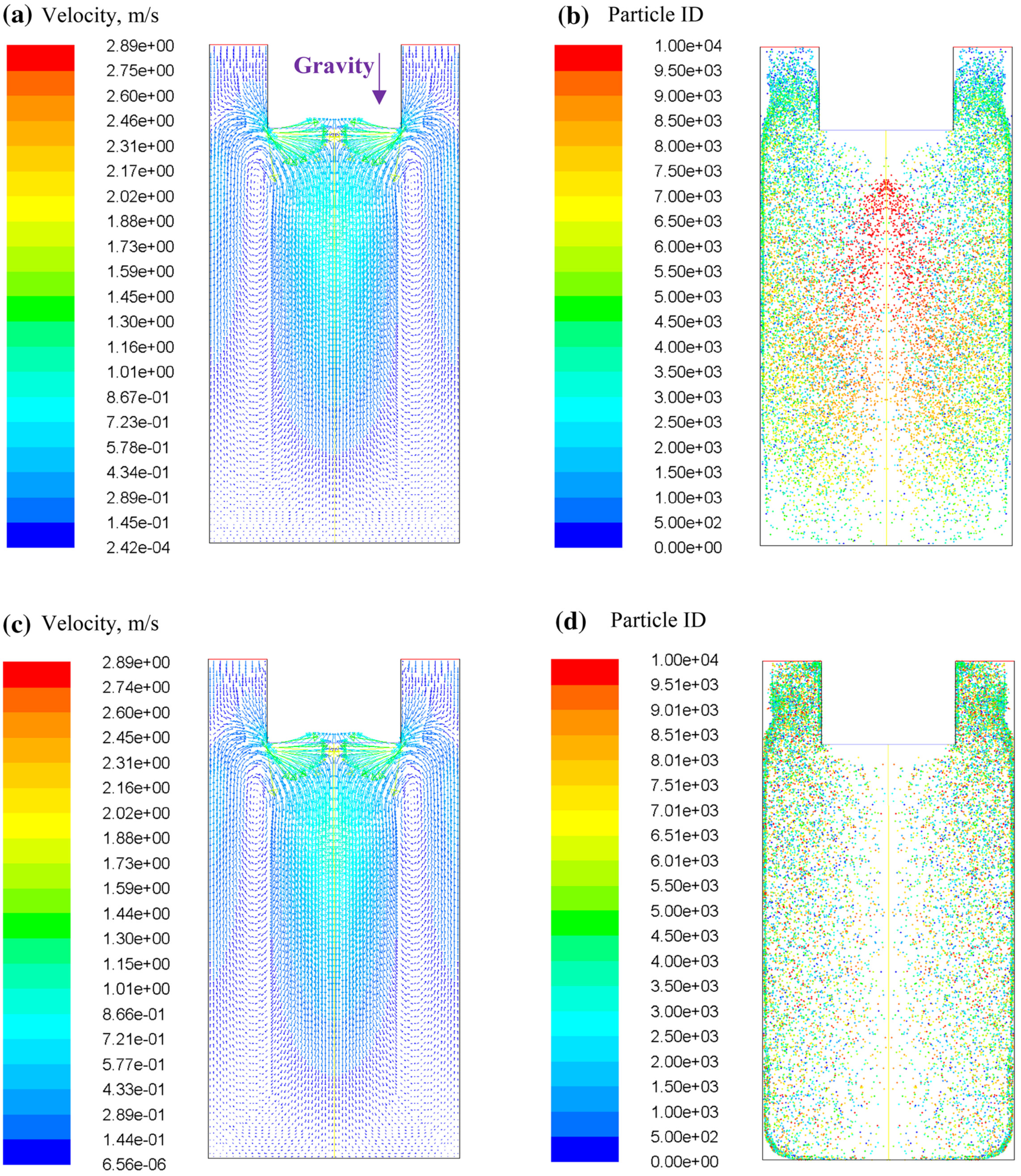

Fig. 4. Fluid flow and particle distributions with EMS: (a) fluid flow after 1.0 s; (b) particle distribution after 1.0 s; (c) fluid flow after 3.0 s; (d) particle distribution after 3.0 s.

$$\mathrm{CSP} = \sum_{i=1}^{N/2} \left| r_i + r_{i+N/2} \right|^2, \qquad (5)$$

where r_i and $r_{i+N/2}$ are vectors from the central atom to a particular pair of nearest neighbors.

In order to study the solidification process, we need to know the equilibrium melting temperature, which is a crucial reference point. A smaller system with dimensions of 6 nm × 6 nm × 20 nm and a Φ^2-nm SiC particle is used to save computational time. Initially, the top 1/4 and the bottom 1/4 atoms are fixed, and the others are melted at the high temperature of 2000 K employing a Nose–Hoover thermostat. Keeping the solid atoms fixed, the liquid atoms are subsequently quenched to an estimated melting temperature and equilibrated over 50 ps. Then, the whole system is allowed to relax up to 500 ps with the temperature maintained at the estimated value of T_m.

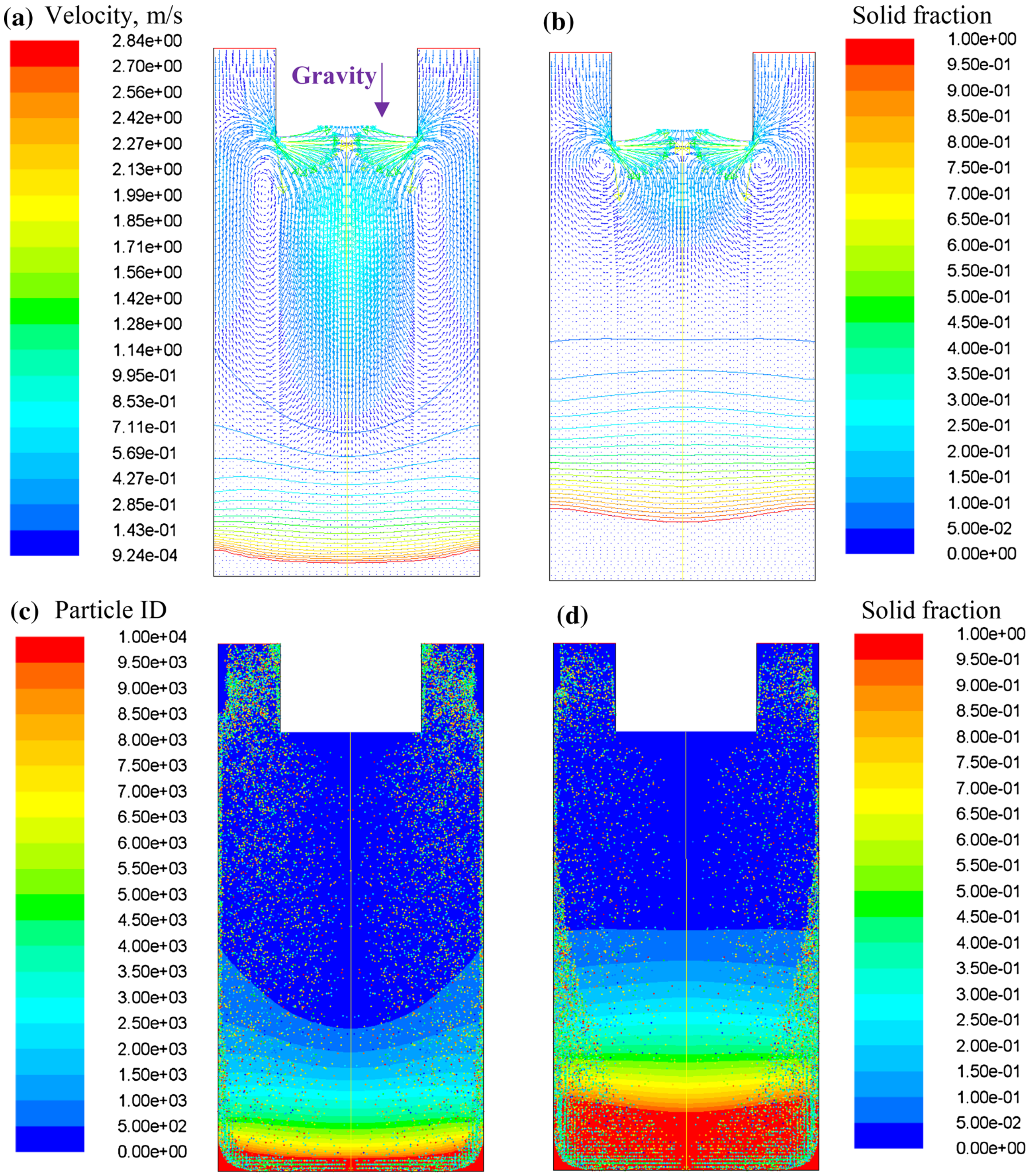

Fig. 5. Fluid flow and particle distributions: (a) fluid flow after 10.0 s; (b) fluid flow after 30.0 s; (c) particle distribution after 10.0 s; (d) particle distribution after 30.0 s.

If T_m is larger than the melting temperature, the whole system will eventually become liquid, otherwise, it will become solid. The equilibrium melting can also be determined from the evolution of potential energy of the solid–liquid coexistence system.[37] Figure 9 shows the evolution of potential energies of the solid–liquid coexistence system at different temperatures. It can be seen that the potential energies increase with time at temperatures above 788 K, indicating that the system is melting, while the potential energies decrease with time at temperatures below 787 K. Thus, the equilibrium melting temperature is estimated to be 787–788 K, which is about 146 K below the theoretical melting temperature of pure aluminium.

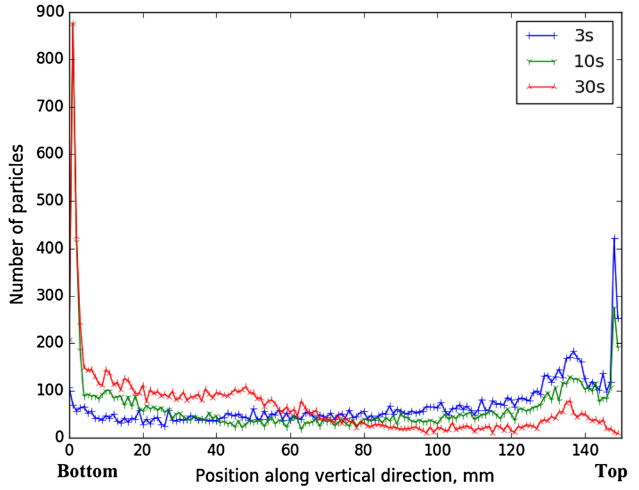

Fig. 6. Particle distribution along vertical direction after 3 s, 10 s, and 30 s.

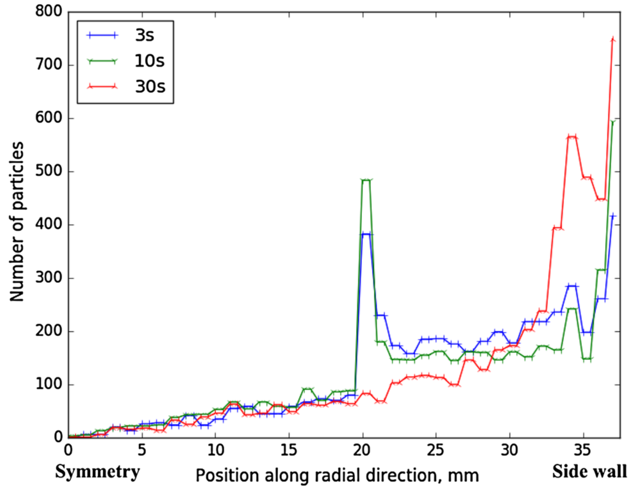

Fig. 7. Particle distribution along radial direction after 3 s, 10 s, and 30 s.

The two-phase Al system is established by holding the atoms fixed in the solid Al region of the original crystalline lattice and melting the liquid Al region by raising the temperature to some temperature above the melting point. The whole system is equilibrated after 40 ps, then the initial solid Al atoms are fixed at some temperature (500 K) below the melting point, and Si, C, and liquid Al atoms with the micro-canonical ensemble (NVE; constant atom number, volume and energy) will "release heat" through the solid atoms. Figure 10 shows the solid–liquid status of the system after 100 ps, 200 ps, 400 ps, and 600 ps, respectively.

As can be seen from Fig. 10a, when the liquid–solid interfaces are far away from the SiC nanoparticle, both of the interfaces at the top and bottom are flat. When the interface at the bottom approaches the SiC nanoparticle, a trough is formed below the particle (see Fig. 10b). As time goes on, the interface at the bottom passes through the particle and the

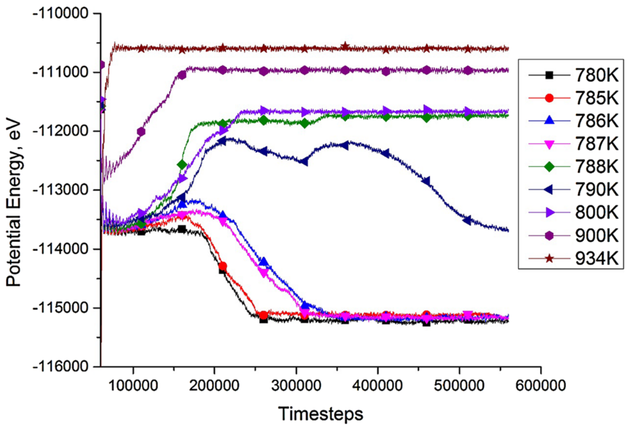

Fig. 9. Evolution of potential energies of the system at different temperatures.

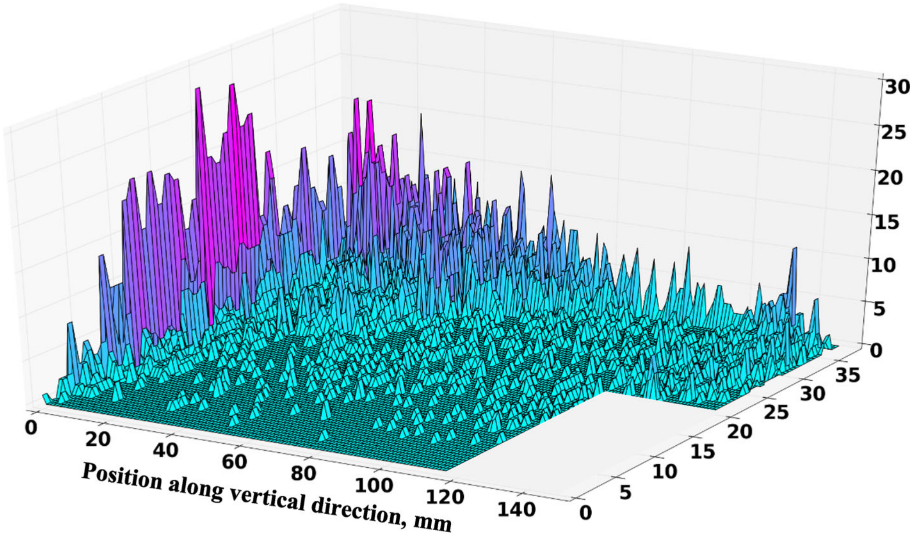

Fig. 8. Overall particle distribution after 30 s.

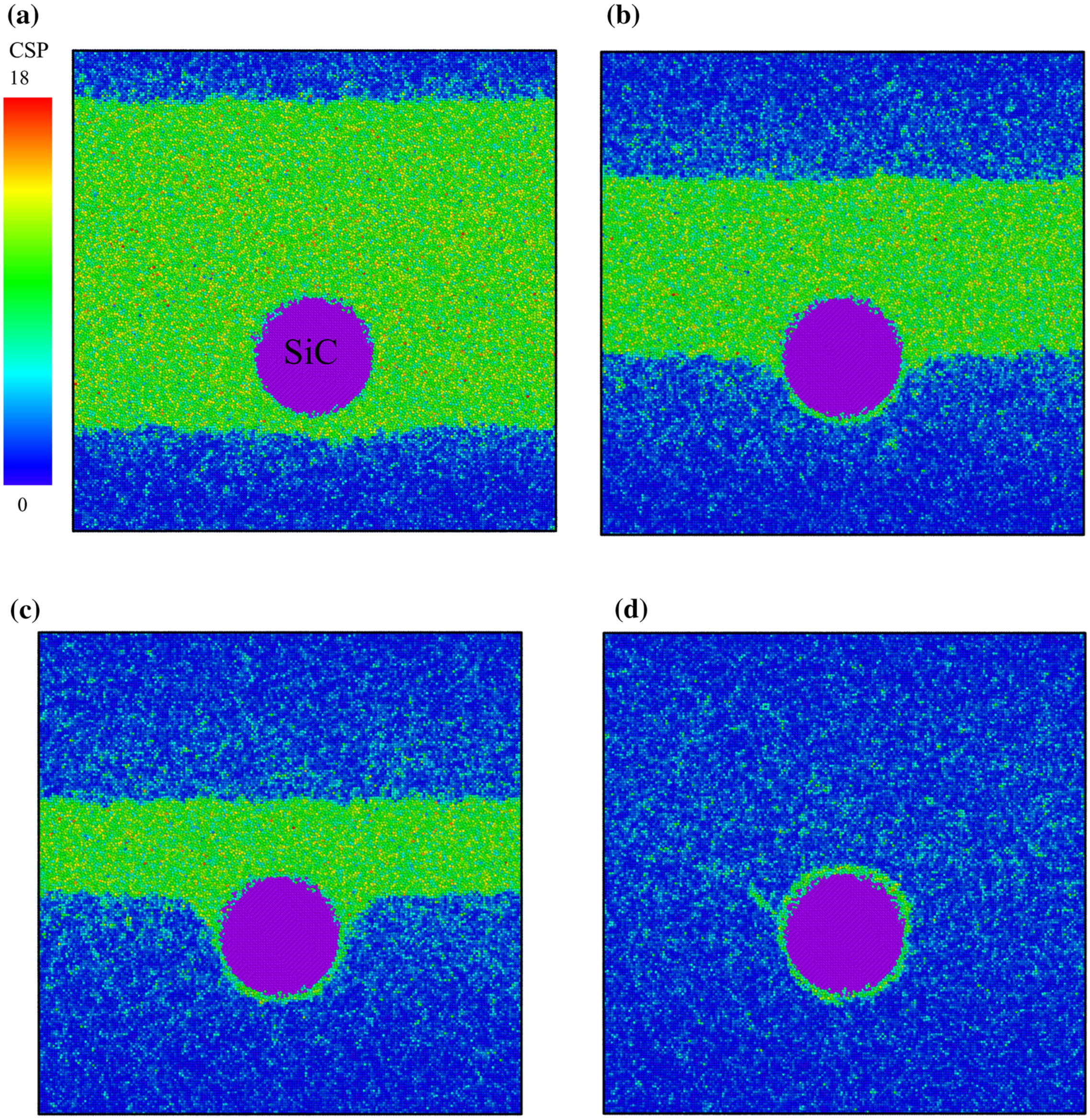

Fig. 10. Solid/liquid status of the system after (a) 100 ps; (b) 200 ps; (c) 400 ps; and (d) 600 ps.

interface at the top approaches the particle (see Fig. 10c). Finally, these two interfaces meet each other, become one, and disappear (see Fig. 10d).

However, we may not notice the movement of the SiC nanoparticle from Fig. 10, because it is extremely small. Figure 11 plots the position of the SiC nanoparticle with time. As can be seen, the horizontal movement (*x* and *y*) of the nanoparticle is negligible. But in the *z* direction (vertical), the particle moves down towards the liquid–solid interface at the bottom in the beginning, and when the interface from the top approaches it, the particle again moves up towards that interface. So it is confirmed during the solidification process that the SiC nanoparticle will be engulfed by the solidification front instead of being pushed.

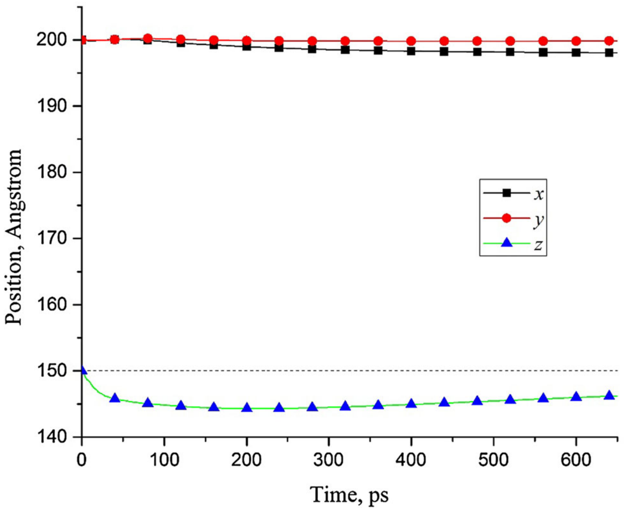

Fig. 11. Position of SiC nanoparticle during solidification.

CONCLUDING REMARKS

A magneto-hydro-dynamics model was developed in ANSYS Maxwell and ANSYS Fluent. The DDPM model coupled with the k–ω turbulence model was used to investigate the distribution of SiC nanoparticles into a 6061 matrix under ultrasonic and induction stirring and molten metal and unidirectional solidification processing conditions. It was demonstrated that induction stirring can help improve the fluid flow characteristics, making the nanoparticle distribution even more uniform.

The complex interactions between a SiC nanoparticle and the Al liquid–solid interface were analysed with a three dimensional (3D) molecular dynamics model using LAMMPS on the High Performance Computing Cluster (HPCC) at the University of Alabama. The assumption that ultrafine particles will be engulfed by the solidification front instead of being pushed was supported by MD simulation.

REFERENCES

1. J.W. Kaczmar, K. Pietrzak, and W. Wlosinski, *J. Mater. Process. Technol.* 106, 58 (2000).
2. K. Durisinova, J. Durisin, M. Orolinova, and M. Durisin, *J. Alloys Compd.* 525, 137 (2012).
3. C.H. William, *Mater. Sci. Eng. A* 244, 75 (1998).
4. Y. Yang, J. Lan, and X. Li, *Mater. Sci. Eng. A* 380, 378 (2004).
5. G. Cao, H. Konishi, and X. Li, *Mater. Sci. Eng. A* 486, 357 (2008).
6. J.H. Shin, H.J. Choi, M.K. Cho, and D.H. Bae, *J. Compos. Mater.* 48, 99 (2014).
7. B. Dikici, M. Gavgali, and F. Bedir, *J. Compos. Mater.* 45, 895 (2010).
8. A.A. El-Daly, M. Abdelhameed, M. Hashish, and W.M. Daoush, *Mater. Sci. Eng. A* 559, 384 (2013).
9. X. Jiang, M. Galano, and F. Audebert, *Mater. Charact.* 88, 111 (2014).
10. J.H. Shin and D.H. Bae, *Mater. Chem. Phys.* 143, 1423 (2014).
11. C. Borgohain, K. Acharyya, S. Sarma, K.K. Senapati, K.C. Sarma, and P. Phukan, *J. Mater. Sci.* 48, 162 (2013).
12. J.B. Ferguson, B.F. Schultz, P.K. Rohatgi, and C.S. Kim, *Light Metals 2014* (John Wiley & Sons, Inc., 2014), pp. 1383–1388.
13. F.K. Sautter, *J. Electrochem. Soc.* 110, 557 (1963).
14. M. Mach, P. Karban, I. Dolezel, and D. Trutwin, in *International Scientific Colloquium*, Riga (Latvia), 203 (2006).
15. R. Schwarze and F. Obermeier, *Model. Simul. Mater. Sci. Eng.* 12, 985 (2004).
16. J.K. Kim and P.K. Rohatgi, *Metall. Mater. Trans. A* 29, 351 (1998).
17. D.R. Uhlmann, B. Chalmers, and K.A. Jackson, *J. Appl. Phys.* 35, 2986 (1964).
18. D.M. Stefanescu, A. Moitra, A.S. Kacar, and B.K. Dhindaw, *Metall. Trans. A* 21, 231 (1990).
19. D. Shangguan, S. Ahuja, and D.M. Stefanescu, *Metall. Trans. A* 23, 669 (1992).
20. G. Kaptay, *Metall. Mater. Trans. A* 32, 993 (2001).
21. Fluent 6.3: User's Guide Manual Fluent Inc. and Ansys's Fluent 2006 http://ansys.com/.
22. S. Plimpton, *J. Comput. Phys.* 117, 1 (1995). http://lammps.sandia.gov.
23. D. Zhang and L. Nastac, *J. Mater. Res. Technol.* 3, 296 (2014).
24. D. Zhang and L. Nastac, *IOP Conference Series: Materials Science and Engineering*, Vol. 84 (IOP Publishing, 2015), p. 012020.
25. D. Zhang and L. Nastac, *Int. J. Cast. Met. Res.* 29, 236 (2016). doi:10.1080/13640461.2016.1144266.
26. C.R. Dandekar and Y.C. Shin, *Compos. Part A Appl. Sci. Manuf.* 42, 355 (2011).
27. B. Chalmers, Melting and freezing. *Trans. Aime* 200, 519 (1954).
28. J. Hoyt, M. Asta, and A. Karma, *Interface Sci.* 10, 181 (2002).
29. Y. Mishin, D. Farkas, M.J. Mehl, and D.A. Papaconstantopoulos, *Phys. Rev. B* 59, 3393 (1999).
30. J. Winey, A. Kubota, and Y. Gupta, *Modell. Simul. Mater. Sci. Eng.* 17, 055004 (2009).
31. J. Tersoff, *Phys. Rev. B* 39, 5566 (1989). doi:10.1103/PhysRevB.39.5566.
32. J. Tersoff, *Phys. Rev. Lett.* 64, 1757 (1989). doi:10.1103/PhysRevLett.64.1757.
33. H. Zhao, N. Chen, and Y. Long, *J. Phys.: Condens. Matter* 21, 225002 (2009).
34. X. Liu, S. Jia, and L. Nastac, *Int. J. Metalcast.* 8, 1 (2014).
35. S. Jia, D. Zhang, and L. Nastac, *J. Mater. Eng. Perform.* 24, 1 (2015).
36. C.L. Kelchner and S. Plimpton, *J. Hamilt. Phys. Rev. B* 58, 11085 (1998).
37. J. Liu and H. Dong, *IOP Conference Series: Materials Science and Engineering*, Vol. 33 (IOP Publishing, 2012), p. 012113.